Optics and Lasers in Engineering 154 (2022) 107047

Contents lists available at ScienceDirect

Optics and Lasers in Engineering

journal homepage: www.elsevier.com/locate/optlaseng

Multi-parameter optical gauge based on mode coupling effect in asymmetric index multi-core fibres

Oskar Arrizabalaga [a,*], Qi Sun [b], Timothy Lee [b], Joseba Zubia [a], Javier Velasco Pascual [c], Idurre SÁez De Ocariz [c], Axel SchÜlzgen [d], Rodrigo Amezcua-Correa [d], Gilberto Brambilla [b], Martynas Beresna [b]

[a] Department of Communications Engineering, University of the Basque Country (UPV/EHU) plaza Ingeniero Torres Quevedo s/n, 48013, Bilbao, Spain
[b] Optoelectronics Research Centre, University of Southampton, Southampton SO17 1BJ, UK
[c] Fundación Centro de Tecnologías Aeronáuticas (CTA), Miñano, Spain
[d] CREOL, The College of Optics & Photonics, University of Central Florida

ARTICLE INFO

Keywords:
Optical gauges
Optical fibre-based sensors
Multicore fibre-based sensors
Multiparameter sensor
Mode coupling effect

ABSTRACT

An optical gauge based on coupled multi-core fiber is proposed and experimentally demonstrated. By using direct laser writing to selectively break the fiber index profile symmetry, asymmetric mode coupling between cores is introduced. This allows to fabricate optical gauges with the ability to detect and differentiate different types of deformation in structures using just a single sensor.

The fabricated optical gauges are compared with calibrated commercial gauges and fiber Bragg gratings as strain, vibration and curvature gauge. The tests indicate superior performance of this novel optical gauge over the commercially available sensors and offer the highest sensitivities. The proposed technology could be key to the fabrication of new fiber-based sensing devices with more capabilities and better features than previously achieved.

Introduction

The development of optical fiber (OF) based sensing technologies is gaining momentum in the modern aeronautical industry for analysing and validating aeronautical structures to tackle the size, weight and power (SWaP) challenges in next generation system designs. OFs can handle high-bandwidth applications, weigh less than copper wire, are immune to electromagnetic interference and are more reliable. One of the great challenges facing the mechanical, aerospace and aeronautical industries is taking large, heterogeneous sets of data collected from sensors, and extracting information that allows the estimation of the physical response of the structures. Another important challenge is to collect relevant data from a structure in a manner that is cost-effective, and respects the size, weight, cost, energy consumption and bandwidth limitations placed on the system. The key concern is the effect of external forces on the structure, which in extreme cases can lead to permanent deformation or even structural collapse. The most common approach for evaluating the effect of external forces on an object is to use strain gauges [1,2]. They measure strain directly, which can be used to indirectly determine stress, torque, pressure, deflection, and many other measurements. Such transducers provide good accuracy, very high long-term stability and good bandwidth suitable for rapid measurements [3]. However, the fact that they can only measure the strain of a point on the surface of a component in a certain direction and cannot perform global measurement, or that only the surface rather than internal strain of the component can be measured, are the main disadvantages of these devices. Over the last few years, optical fibre sensors (OFSs) have emerged as an optical alternative to electronic strain gauges. OFSs offer many advantages, such as immunity to electromagnetic interference and high voltage, low hazard potential, immunity to lightning strikes, capability of remote sensing and small size. The most popular optical strain gauges are based on fibre Bragg gratings (FBGs) [4,5]. Compared to traditional electrical strain gauges, optical strain gauges do not need electricity. Instead, the technology is based on light that propagates through a fibre. Therefore, the sensors are completely passive and immune, for example, to electromagnetic interference. This is just one of the reasons why optical strain gauges are superior to electrical ones in certain applications. However, thermal and transversal strain sensitivities, high-cost for building and maintaining, limited supplies and the difficulty in demodulating wavelength shift are the main drawbacks of FBG based strain monitoring [6,7].

Although several optical fibre-based technologies [8,9] have been developed in order to overcome these limitations, only FBGs have emerged as a commercially successful solution. Nevertheless, there are

* Corresponding author.
E-mail address: oskar.arrizabalaga@ehu.eus (O. Arrizabalaga).

https://doi.org/10.1016/j.optlaseng.2022.107047
Received 31 October 2021; Received in revised form 7 March 2022; Accepted 14 March 2022
Available online 22 March 2022

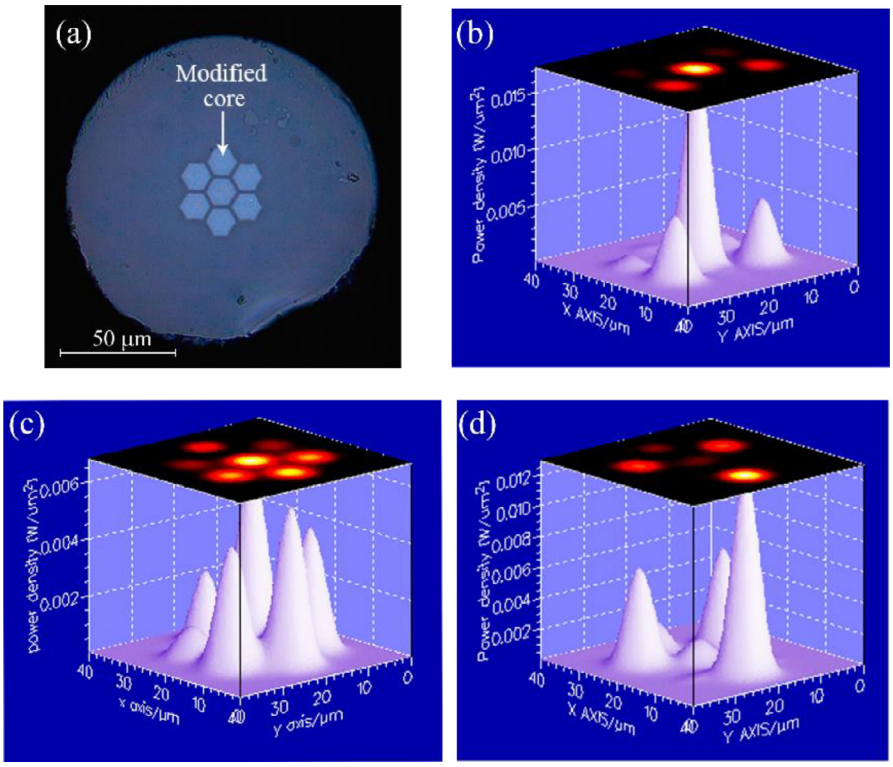

Fig 1. (a) Micrograph of the cross section of the ACMCF. (b), (c) and (d) Simulated mode power density profiles from a full vector finite-element mode solver (Photon Design, Oxford, UK) of SM_1, SM_2 and SM_3 supermodes, respectively.

other approaches that have not yet been properly exploited; e.g. the exchange of light between cores in strongly coupled multi-core fibre [10] (SCMCF) is extremely sensitive to external influences such as strain. This is normally called the mode coupling [11] (MC) effect, and the application of this theoretical basis in SCMCFs could be the key to developing a new generation of optical fibre based sensing devices.

In this work, optical gauges are fabricated by tailoring the refractive index profiles of the peripherical cores in a short piece of SCMCF, providing an asymmetric effective index with respect to a plane of symmetry. This causes an asymmetric MC effect with respect to the aforementioned plane enabling us to implement optical gauges capable of detecting different mechanical deformations such as strain, vibrations or curvature with high sensitivity using only a single gauge. This device provides advantages that include ultrahigh sensitivity, wide detection range and good stability. For all these reasons, this new approach could be key to the fabrication of new fibre-based optical gauges with more capabilities and better features than previously achieved.

Theoretical model and experimental setup

A new class of sensing devices and sensors exploiting asymmetric coupled multi core fiber (ACMCF) is developed here. In the multicore fiber, a central core is surrounded by another six cores made of silica doped with germanium and embedded in pure silica cladding (see Fig. 1(a)). The numerical aperture of the cores at $\lambda = 1.55$ μm is NA=0.14, close to that of a standard SMF. The radius of each core is 4.5 μm with a core-to-core pitch (Λ) of 11 μm. All the cores, except one of the surrounding cores, have the same refractive index. This external core was modified by femtosecond laser direct writing to increase the refractive index of a selected volumetric region within the fiber.

The laser-modified region has a size of 10 μm × 10 μm × 4 cm, which ensures to cover one of the fiber cores. The laser system Pharos (Light Conversion Ltd., Lithuania) operates at λ~1030 nm, with a pulse duration of 200 fs and a repetition rate of 200 kHz. For enhancing writing resolution, laser writing was carried out using the second harmonic at λ~515 nm. The laser writing power was set to 6 mW after the 0.4 NA objective, which corresponds to a laser pulse energy of 30 nJ (due to the presence of dopants in the fibre, this energy is lower than for pure silica which would typically be up to 100 nJ). Since the main purpose of the laser processing was to break the symmetry of the fibre core region, the modified region does not require uniform induced stress and so the basic multiscan writing pattern was applied [12] (where the laser scanlines were inscribed consecutively one next to the other). The pulse density was 3×10^5 pulses/mm along each scanline, and the separation

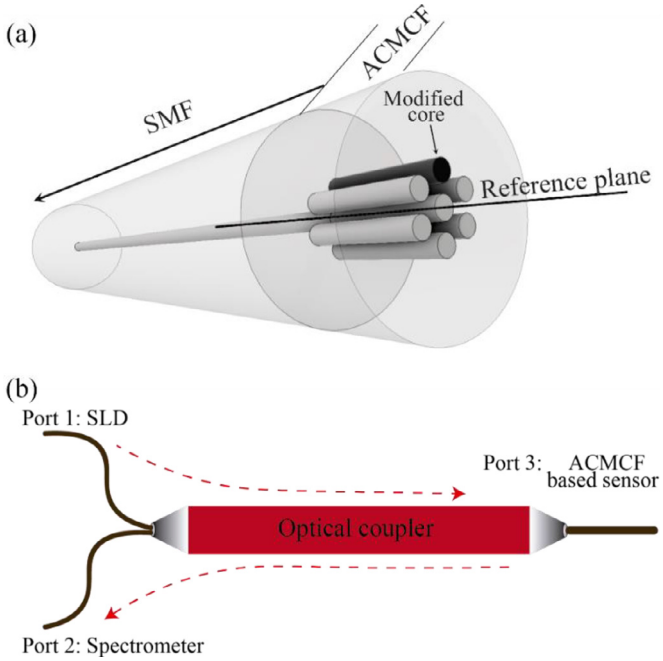

Fig 2. (a) Schematic representation of the sensing device structure. (b) Experimental setup. SLD denotes superluminescent diode.

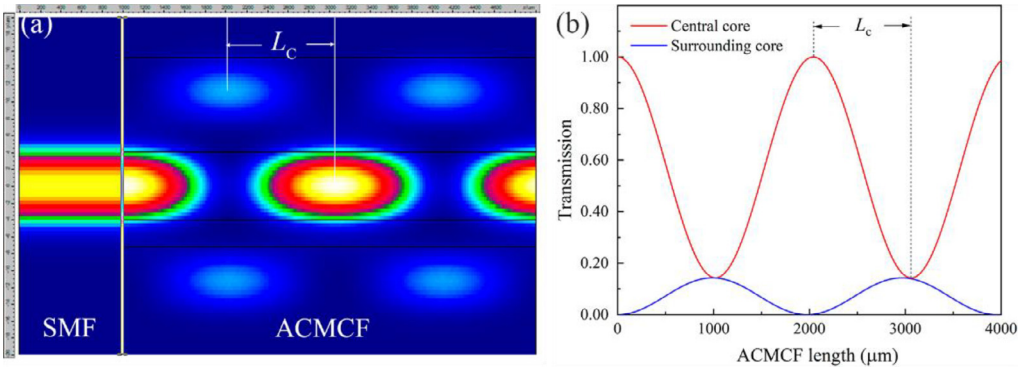

Fig 3. (a) Simulated power distribution profile along length of 4 mm ACMCF. (b) Simulated power in the central and surrounding cores vs distance along ACMCF.

between scanlines was 200 nm. With the help of the monitoring camera, it is possible to resolve the edges of the cores when focusing at different heights, and the fibre can be positioned with high repeatability using the laser writing stages to ensure the pulses focus into one of the non-central cores. In fact, since the fibre index symmetry can be broken even with the modified region only partially inscribed in the core, the writing process has a large positioning tolerance.

The ACMCF (Fig. 1) supports seven modes, each of which has two orthogonal linear polarizations (x and y). These modes can be categorized as fundamental modes, higher order modes with a central peak (Fig. 1(b) and (c)) and higher order modes without central peak (Fig. 1(d)). These modes are normally called supermodes [13] and have been labelled them as SM_1, SM_2 and SM_3, respectively. The sensing device structure consists of a short (ACMCF) segment, axially aligned and spliced onto an end face of a standard SMF-28 single mode fibre (SMF), as can be seen in Fig. 2. Then, when the fundamental mode (FM) from the SMF is launched into the central core of the ACMCF, the FM power couples largely into the SM_1 and SM_2 modes. As these two supermodes travel through the central core of the ACMCF, the propagation constant mismatch between SM_1 and SM_2 causes periodic interference between them and due to the phase mismatch, the power in the central core will show beating as in Fig. 3.

The mode amplitudes in the central core A_{cc} and surrounding cores A_{sc} at distance L in the ACMCF can be obtained from the following equations [14,15]:

$$A_{cc}(L) = \left[\cos CL + \frac{j}{\sqrt{7}}\sin CL\right] e^{-jCL\frac{1}{\sqrt{7}}} \tag{1}$$

$$A_{sc}(L) = \left[-\frac{j}{\sqrt{7}}\sin CL\right] e^{-jCL\frac{1}{\sqrt{7}}} \tag{2}$$

Where C is the coupling coefficient between a propagation mode for circularly distributed cores and a propagation mode for a central core (see Fig. 3). This coefficient depends on the number of distributed cores m, the separation between cores Λ, and the difference between the propagation constants of the SM_1 and SM_2, β and, it can be calculated by means of the following equation:

$$C = \sqrt{m}\frac{\Delta\beta}{2} = \sqrt{7}\frac{(\beta_{SM_1} - \beta_{SM_2})}{2} \tag{3}$$

Being the propagation constant defined as $\beta_{SMx} = (2\pi/\lambda)\, n_{eff\,SMx}$ where n_{eff} is the effective index for the propagating mode Eq. (3). can be rewritten as:

$$C = \sqrt{7}\frac{2\pi}{\lambda}\Delta n_{eff}. \tag{4}$$

Then, the normalised power in the central core P_{cc} can be expressed as:

$$P_{cc}(L) = |A(L)|^2 = \frac{1}{7} + \frac{6}{7}\cos^2 CL \tag{5}$$

and the normalised power in the surrounding cores is given by:

$$P_{sc}(L) = |A(L)|^2 = \frac{1}{7}\sin^2 CL \tag{6}$$

which are periodic in L and the maximum of P_{cc} will be located at the minimum of P_{sc} as it can be seen in Fig 3(b). According to the Eqs. (5) and (6) the distance between P_{cc} and P_{sc} maximum, is defined

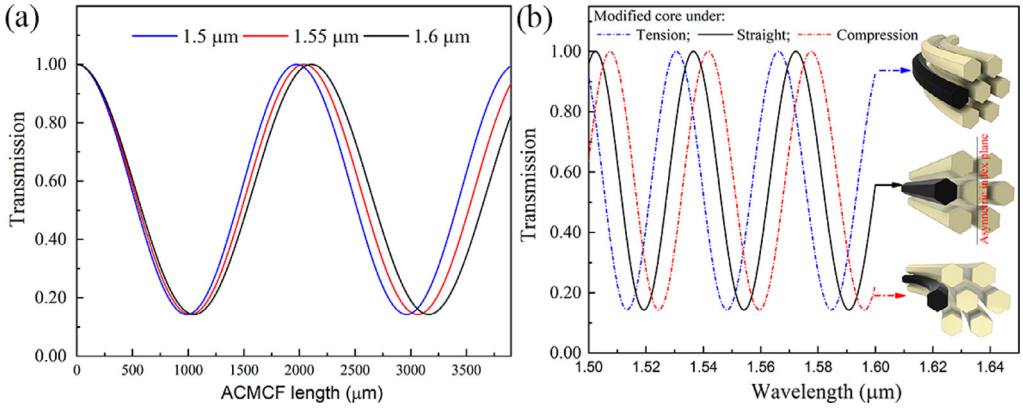

Fig 4. (a) Simulated power distribution along the central core of ACMCF for different wavelengths. (b) Theoretical spectrum of the ACMCF for different mechanical stress types on modified core.

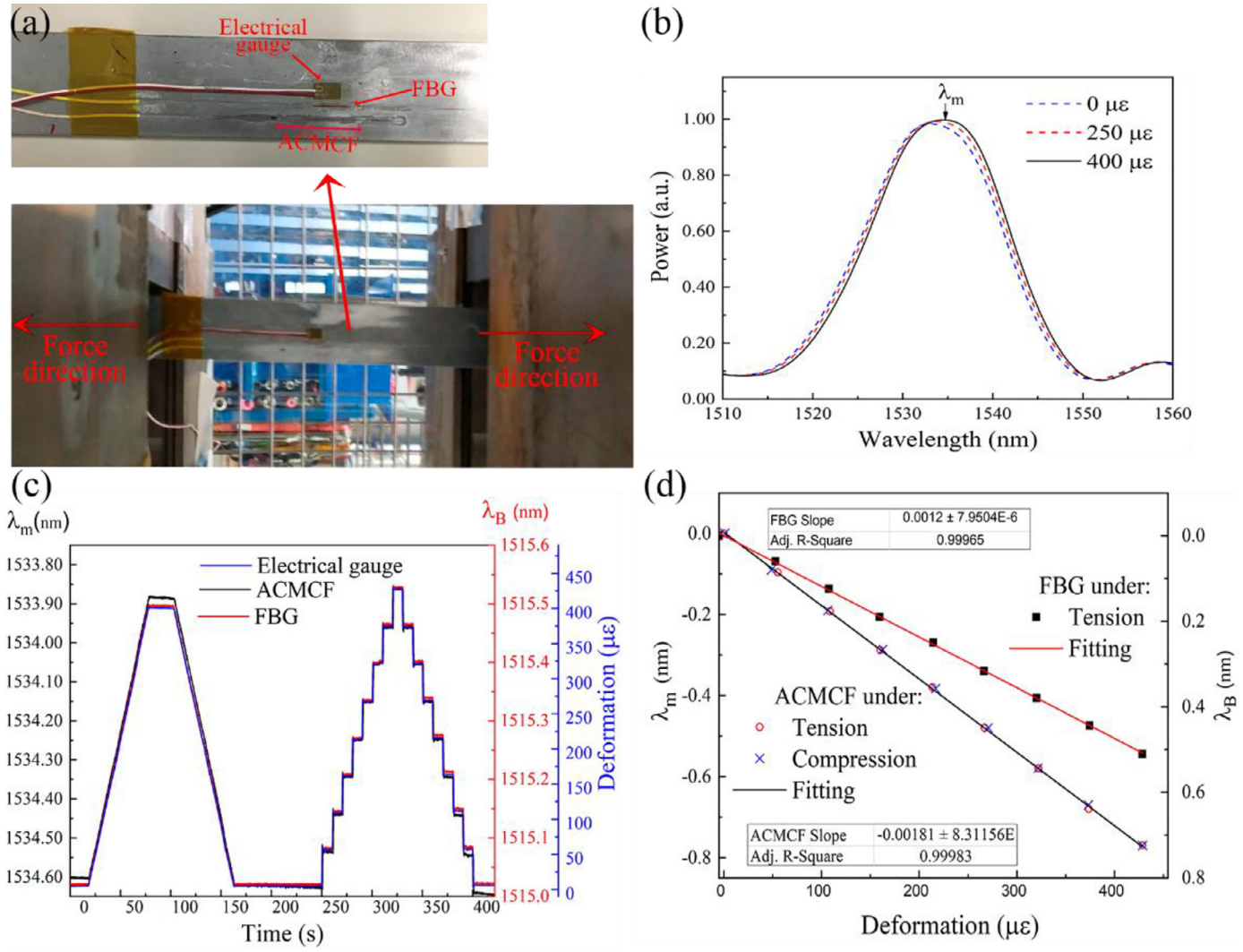

Fig 5. (a) Tensile-compression tests. (b) Measured power spectrum showing peak wavelength shift as the strain increases. (c) Comparison of the ACMCF gauge sensor with the commercial sensors. (d) Comparison of calibration curves between the ACMCF gauge and a commercial FBG.

as the coupling length, L_C and is given by:

$$L_C = \frac{\lambda}{2\sqrt{7}\Delta n_{eff}} \tag{7}$$

According to Eq. (5), the transmission power of the central core reaches a maximum when the phase condition satisfies $(7^{1/2})CL = m\pi$ (m is a positive integer). Therefore, the corresponding wavelength with maximum power λ_m will be located at:

$$\lambda_m = \frac{2m\pi}{\sqrt{7}\frac{\partial C_{(\lambda)}}{\partial \lambda}L} \text{ with } m = 1, 2, 3 \tag{8}$$

As it can be deduced from the Eq. 7, and it is shown in Fig.3(a), the L_C is wavelength dependent. Repeating the Eq. (5) calculations for different wavelengths, a periodically modulated spectrum at the output of the system is obtained (Fig. 4(b)).

On the other hand, the deformation type, e.g. curvature, tension or compression of the ACMCF causes variation in the index and/or length (L) of the cores. According to the elastic-optic effect, the index change of the cores can be expressed through equivalent refractive index model [16]:

$$n'(x,y) = n(x,y)\left[1 - \frac{n(n,x)^2 x}{2R}(P_{12} - \nu(P_{11} + P_{12}))\right]\exp\left(\frac{x}{R}\right) \tag{9}$$

with n(x,y) being the refractive index of the straight ACMCF, P_{11} and P_{12} are components of the elasto -optical tensor, υ is Poisson's ratio, R is the radius of curvature and x is distance from center of fiber. This transformation allows a circularly curved ACMMF segment to be modelled as an equivalent straight one.

Then, when the ACMCF is subjected to any type of deformation (D_T), λ_m will shift according to the following equation:

$$\frac{\partial \lambda_m}{\partial D_T} = \left[\frac{1}{\Delta n_{eff}} \cdot \frac{\partial C}{\partial \Delta n_{eff}} + \frac{1}{L} \cdot \frac{\partial \lambda_m}{\partial L}\right] \cdot \lambda_m \tag{10}$$

Where $\partial C/\partial \Delta n_{eff}$ is the variation of the coupling coefficient C due to the changes of the index of the cores caused by the deformation and $\partial \lambda_m/\partial D_L$ is the variation of λ_m due to changes of the length of the specimen caused by the deformation.

In the ACMCF, due to the asymmetrical distribution of the index of the cores with respect to a reference plane, Δn_{eff} will be different depending on whether the modified core is under tension or compression. In addition, the length of the ACMCF segment will be longer or shorter depending on whether it is under axial expansion or axial compression. Consequently, the coupling length L_C will vary and, therefore, the variation of the λ_m will be a function of both types of deformation as shown in Eq. (10).

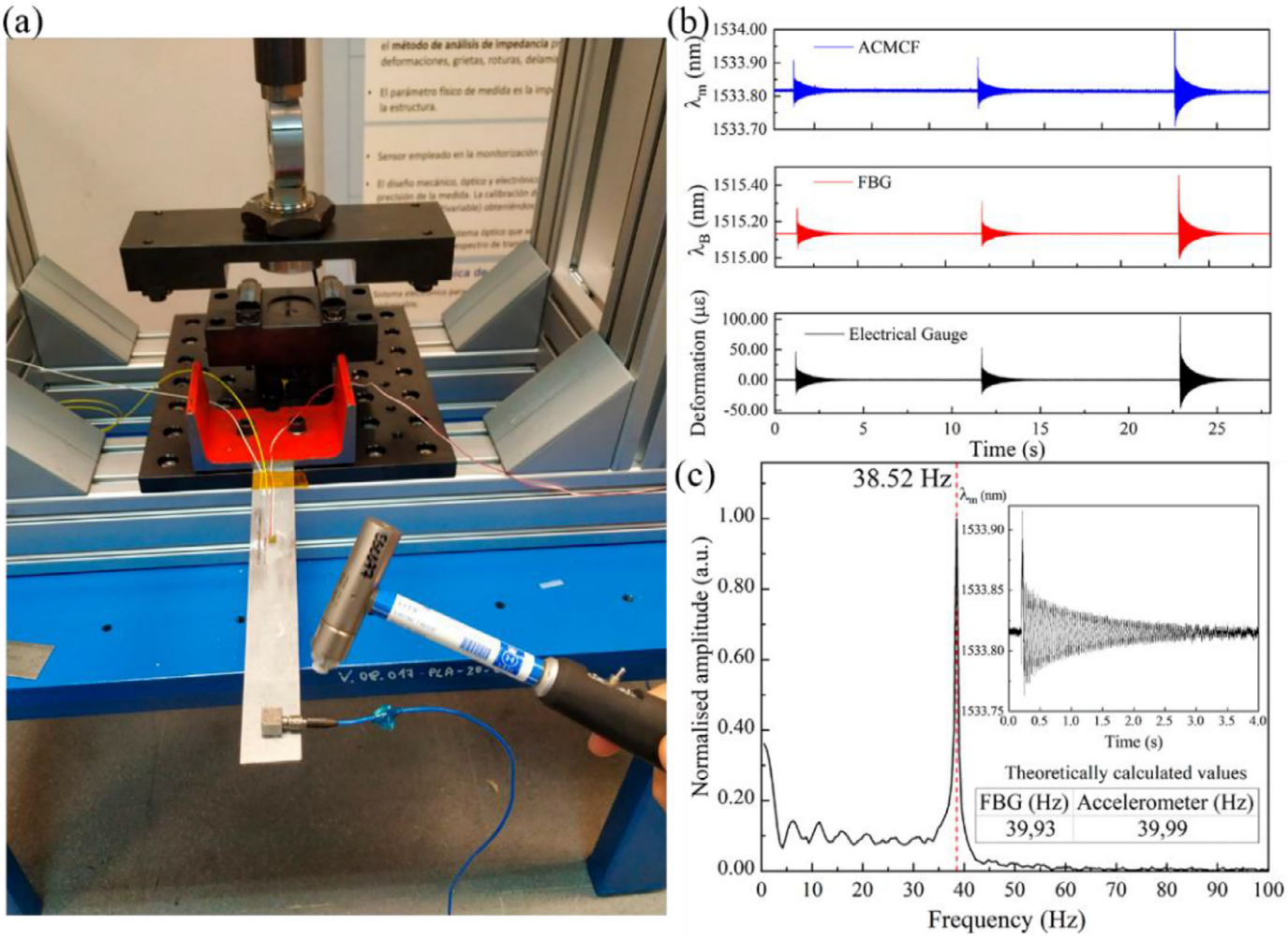

Fig 6. Experimental setup for subjecting the specimen to a static four-points bend loading test. The ACMCF gauge along with commercial sensors were placed on top of the sample.

Experimental setup and results

Experimental tests aimed at evaluating ACMCF performance in representative structural tests: tensile, compression, modes of vibration and four point bending. The measurement setup for carrying out the experimental tests is shown in Fig. 2(b). A superluminescent diode (SLD) was used as a broadband light source centred at 1550 nm. The reflected spectrum from the ACMCF sensor was collected in real-time by means of a miniature interrogation monitor (Ibsen Photonics, Denmark) (Fig. 5(b). To measure the deformation of the specimen the local peak of the spectrum (λ_m) was tracked.

The device was experimentally assessed as an optical strain gauge. To do that, a ~ 4 cm segment of ACMCF with a modified core was placed in such a way that the index of the surrounding cores was asymmetrical with respect to a reference plane [17], and bonded to a steel plate of 325 × 25 × 3 mm. To place the ACMCF with asymmetric index with respect to a reference plane (see Fig. 2(a)), first, the SMF-ACMCF was connected to the experimental setup (see Fig. 2(b)) and the collected spectrum was analysed with a spectrometer (from Ibsen Photonics). Afterwards, the SMF was secured to a precision fibre rotator leaving the segment composed of ACMCF in free space. The whole assembly was fixed to a flexure precision stage with a stepper motor actuator. The next step was to place the fibre with the written core in a symmetrical position with respect to the bending plane. To do this, the SMF was fixed and translated in the ± x-axis with the flexure precision stage. Simultaneously, the fibre was rotated to find the position, where the spectrum shift is the same regardless of whether the displacement is on the ±x-axis or on the –x-axis. Then, the fibre was rotated ±90° from the reference position, the written core is placed in such a way that it lies in the bend plane, so the fibre index profiles for left and right bends are no longer identical. Thus, according, positive or negative bending on the fibre will cause the largest spectral shifts to shorter or larger wavelengths and enabling to detect the magnitude and direction of the bending. In the direction that the spectrum shifts to shorter wavelengths, the modified core is under tension (Positive curvature; Fig 7(b)), and conversely, in the direction that the spectrum shifts to longer wavelengths, the modified core will be under compression (Negative curvature; Fig 7(c)). Afterwards, the ACMCF segment was transferred to the specimen and was covered along the whole length with a cyanoacrylate adhesive and left to cure for twenty four hours.

Then, in order to compare the ACMCF sensor with its commercial counterparts, a commercial FBG and a strain gauge was bonded close to the ACMCF sensing device, as can be seen Fig. 5(a).

The evaluation of the ACMCF sensor was carried out at constant temperature (25 °C) in a fatigue test bench at the Aerospace Technology Centre (Miñano, Spain). Tensile and compression test consisted of subjecting the ACMCF to axial tensile stress by means of a computer-controlled hydraulic system (servocylinder hydraulic, model CIL125/80/80 × 500). The experiments were carried out with different samples of ACMCF several times on different days.

Fig. 5(b) shows the reflection spectra obtained from the ACMCF sensor and at different levels of loads applied to the sample. The shift of

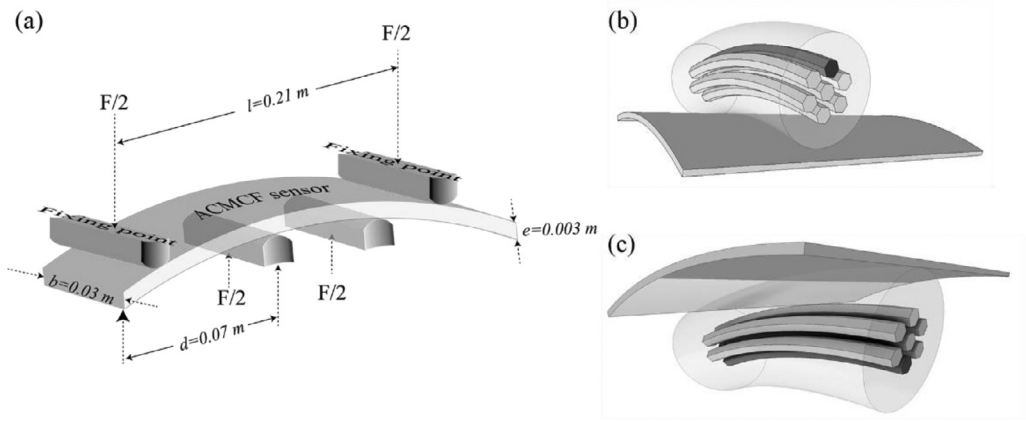

Fig 7. (a) Schematic illustration of the static four-points bend loading test. (b) ACMCF when the sample is under positive curvature and (c) negative curvature.

the maximum peak $\Delta\lambda_m$ was calculated by means of the centre of gravity algorithm [18,19] which is capable of detecting pico-meters shifts Fig. 5(c) shows the comparison between the ACMCF device and its commercial counterparts when the sample is subjected to several tension-compression cycles and confirms that the ACMCF device is capable of following the tension-compression steps with as much accuracy as its commercial counterparts. The calibration curve, shown in Fig. 5(d), gave us the relationship between strain and wavelength shift. The sensitivity of the ACMCF sensor was found to be 1.81 pm/$\mu\varepsilon$ whereas the sensitivity of the FBG was found to be 1.2 pm/$\mu\varepsilon$. The ACMCF sensor showed a 33 % higher sensitivity than the FBG. It should also be noted that the ACMCF sensing device does not exhibit hysteresis.

The ACMCF device also was assessed as a vibration sensor. This evaluation was carried out in static conditions, using an impact hammer (Dytran, model 5850B) as excitation mechanism and a piezoelectric accelerometer (PCB, model 333B32) as reference sensor. To carry out the test, the specimen was tied at 80 mm from one of its ends, considering it a fixed support (see Fig. 6(a)).

Fig. 6(b) shows the comparison between the ACMCF device and its commercial counterparts when the sample is subjected to three consecutives impacts. From the aforementioned graphic, it can be seen that the ACMCF device behaves similar to its commercial counterparts. The inset in Fig. 6(c) shows the response of the ACMCF sensor to a hammer impact and also shows the fast Fourier transform (FFT) of the spectral response of the ACMCF device, demonstrating that the first natural frequency measured by the ACMCF device practically matches with the theoretical value calculated.

In order to evaluate the ACMCF sensing device as a curvature gauge, the sample was subjected to a static four-points bend loading test (Fig. 7(a) and 8). This test provides load versus deflection results and strain measurements [20]. The objective of this test is to demonstrate an important breakthrough of the ACMCF device, which is to distinguish the direction of the curvature with just one sensor. The tests were carried out at the CTA facilities, by means of a four-point load machine (Festo, CMMT-AS).

The positive bend direction was defined as the deformation experienced when all three sensors are positioned on the top of the sample (see Fig. 7(b), 8). A change in the bending direction was simulated by flipping the sensor, i.e. the negative curvatures were measured when the sample was flipped and the sensors were at the bottom (see Fig. 7(c)).

The first test consisted of subjecting the sample to a positive curvature. Then, from the fixation points, a progressive load, from zero to 350 N, was applied to the sample causing it to bend (see Fig. 7(a)). Because the modified core was positioned orthogonally with respect to the flexion direction, it will undergo tension when subjected to positive curvature (see Fig. 7(b)). On the contrary, it will undergo compression when subjected to negative curvature (see Fig. 7(c)).

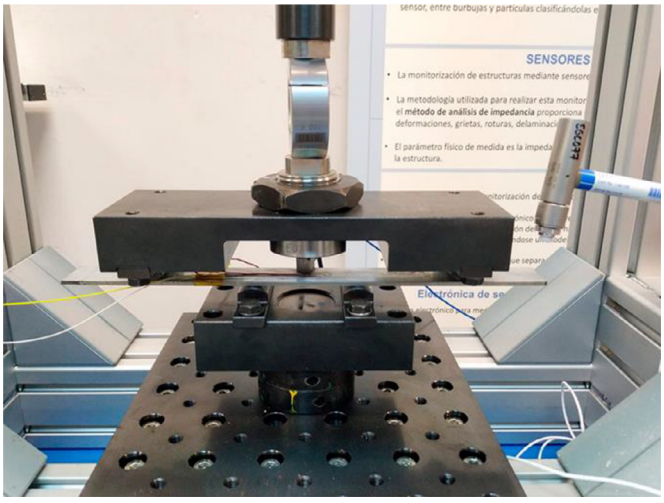

Fig. 8. Experimental setup for subject ing the specimen to a static four-points bend loading test. The ACMCF gauge along with commercial sensors were placed on top of the sample.

Bending causes two effects on the maximum peak of the spectrum λ_m (Fig. 5(b)). On one hand, λ_m will vary due to changes in the length (strain, $\Delta\lambda_\varepsilon$) of the ACMCF; on the other hand, λ_m will vary due to changes in the refractive index of the cores (curvature, $\Delta\lambda_{\sigma c}$). Therefore, the total change of the maximum peak of the spectrum $\Delta\lambda_{mT}$ will vary as:

$$\Delta\lambda_{mT} = \Delta\lambda_{\sigma c} + \Delta\lambda_\varepsilon = \left[\frac{1}{\Delta n_{eff}} \cdot \frac{\partial C}{\partial \Delta n_{eff}} + \frac{1}{L} \cdot \frac{\partial \lambda_m}{\partial L}\right] \cdot \lambda_m. \tag{11}$$

Fig. 8. Experimental setup for subjecting the specimen to a static four-points bend loading test. The ACMCF gauge along with commercial sensors were placed on top of the sample.

The calibration of Fig. 5(d)shows that the device varies ± 0.018 nm/$\mu\varepsilon$ when the deformation is exclusively axial ($\Delta\lambda_\varepsilon$),thus, $\Delta\lambda_\varepsilon(nm) = \pm 0.0018 \cdot \varepsilon$ (red shift if compression, and blue shift if tension). Therefore, the wavelength shift caused strictly by the curvature can be calculated as$\Delta\lambda_{\sigma c}(nm) = \lambda_{mT} - \lambda_\varepsilon$. The curvature can be calculated from the measured strain as follows [21]:

$$\sigma_c(m^{-1}) = \frac{\varepsilon \cdot 2}{e} \tag{12}$$

where e is the thickness of the specimen (see Fig. 8. (a) Fig. 9. shows the graphs with the wavelength shift strictly due to changes in index ($\Delta\lambda_{\sigma c}$) versus deformation and curvature. These graphs demonstrate the strong effect of the asymmetrical distribution of the index of the cores on

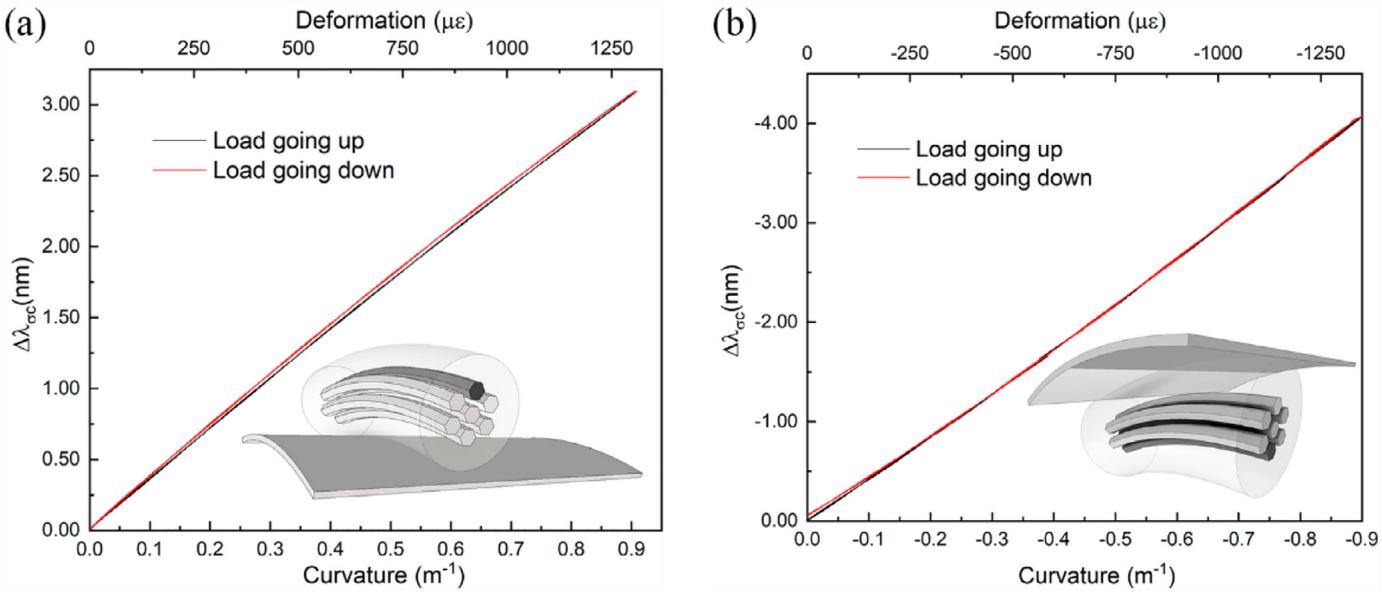

Fig. 9. Wavelength shift strictly due to changes in index ($\Delta\lambda_{\sigma c}$) versus deformation and curvature for (a) positive curvature and (b) negative curvature.

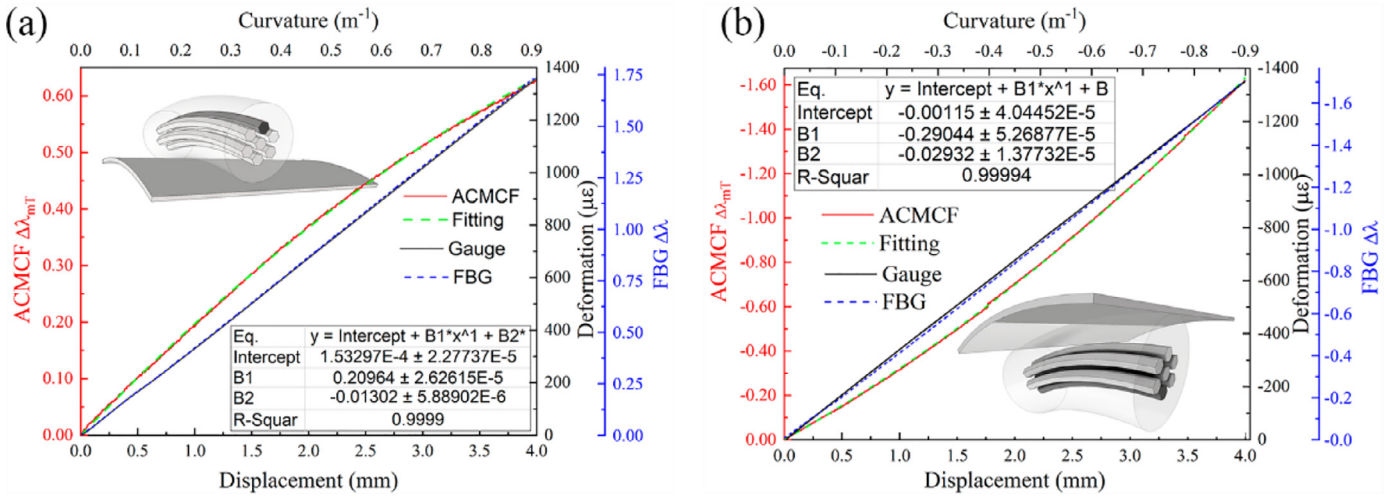

Fig 10. Comparison between the ACMCF gauge, the FBG and the electrical gauge when the sample was subjected to (a) positive and (b) negative curvature.

the wavelength shift. Depending on the direction of the curvature, the effective index of the cores will be different. The spectrum blue shifts or red shifts depending on the curvature orientation. The ACMCF spectrum red shifts at a rate of ~ 3.4 nm/m^{-1} when subjected to tension and blue shifts at ~ 4.4 nm^{-1} when subjected to compression.

The aforementioned figures demonstrate what Eqs. (7) and (8) predict, which is that changes in ACMCF index cause stronger variations in coupling length (C_L) than changes in its length. Therefore, in the proposed optical gauge, the modified core is the key to obtaining different effective index in the ACMCF depending on whether the modified core is under tension or compression: opposite direction wavelength shifts are obtained for each case.

Fig. 10 shows response curves that compare the ACMCF sensor with its commercial counterparts when the specimen was subjected to curvature. In Fig. 10(a), it can be seen how the maximum tracked peak λ_{mT} red shifts in a nonlinear function whereas in the case of axial deformation λ_m shifts linearly (see Fig. 5(d)). On the contrary, when the specimen was subjected to negative curvature (Fig 9(b)), λ_m blue shifts as a nonlinear function.

It should be noted at this juncture that while the commercial ones change linearly regardless of whether the specimen is subjected to curvature or axial deformation, the proposed ACMCF sensor is capable of distinguishing between these two types of deformation. It is an important breakthrough in respect to its commercial competitors.

Conclusions

The asymmetric coupling effect demonstrated in this paper can become the key part for the next generation of high level structural sensing devices. The proposed ACMCF optical gauge has demonstrated the ability to monitor several different physical parameters and clearly differentiates them. Compared with its commercial counterparts as a strain and vibration sensor, the asymmetrically coupled multi core fibre sensor outperformed them by providing 30% higher sensitivity. An important breakthrough of the ACMCF proposed sensor is its ability to simultaneously monitor curvature and its direction.

The ACMCF sensor has the advantages of high repeatability, low-cost, straightforward and reproducible fabrication, and does not have hysteresis.

Author Statement

All authors agree with the submission; that the work has not been published or submitted for publication elsewhere, either completely or in part, or in another form or language; and that no materials are reproduced from another source.

Declaration of Competing Interest

The authors declare that they have no known competing financial interests or personal relationships that could have appeared to influence the work reported in this paper.

Funding

This work has been funded in part by the Fondo Europeo de Desarrollo Regional (FEDER), in part by the Ministerio de Ciencia, Innovación y Universidades under projects RTI2018-094669-B-C31 in part by the GobiernoVasco/Eusko Jaurlaritza ELKARTEK KK-2021/00092 and ELKARTEK KK-2021/00082. The authors also acknowledge UKRI for partial support through research grants EP/S013776/1; NE/S012877/1; NE/T005890/1

References

[1] Higson GR. Recent advances in strain gauges. J. Sci. Instrum. 1964;41(7). doi:10.1088/0950-7671/41/7/301.
[2] Rite E. Strain Gauge Principle, Types, Features and Applications. J. Nippon Med. Sch. 2019;39(2).
[3] Motra HB, Hildebrand J, Dimmig-Osburg A. Assessment of strain measurement techniques to characterise mechanical properties of structural steel. Eng. Sci. Technol. an Int. J. 2014;17(4). doi:10.1016/j.jestch.2014.07.006.
[4] Hill KO, Meltz G. Fiber Bragg grating technology fundamentals and overview. J. Light. Technol. 1997. doi:10.1109/50.618320.
[5] Ma Z, Chen X. Strain transfer characteristics of surface-attached FBGs in aircraft wing distributed deformation measurement. Optik (Stuttg) 2020;207. doi:10.1016/j.ijleo.2020.164468.
[6] Huang Ji-Ying, Van Roosbroeck Jan, Vlekken Johan, Martinez Antonio Bueno, Geernaert Thomas. Francis Berghmans, Bram Van Hoe, Eric Lindner, and Christophe Caucheteur, "FBGs written in specialty fiber for high pressure/high temperature measurement. Opt. Express 2017. doi:10.1364/oe.25.017936.
[7] Zhou Z, Graver T, Hsu L, Ou J. Techniques of Advanced FBG sensors: fabrication, demodulation, encapsulation and their application in the structural health monitoring of bridges. Pacific Sci. Rev. 2003.
[8] Duan DW, Rao YJ, Hou YS, Zhu T. Microbubble based fiber-optic Fabry-Perot interferometer formed by fusion splicing single-mode fibers for strain measurement. Appl. Opt. 2012. doi:10.1364/AO.51.001033.
[9] Zhang Peng, Tang Ming, Gao Feng, Zhu Benpeng, Fu Songnian, Ouyang Jun, Shum Perry Ping, Liu Deming. Cascaded fiber-optic Fabry-Perot interferometers with Vernier effect for highly sensitive measurement of axial strain and magnetic field. Opt. Express 2014. doi:10.1364/oe.22.019581.
[10] Saitoh K, Matsuo S. Multicore fiber technology. J. Light. Technol. 2016. doi:10.1109/JLT.2015.2466444.
[11] Yamashita E, Ozeki S, Atsuki K. Modal Analysis Method for Optical Fibers with Symmetrically Distributed Multiple Cores. J. Light. Technol. 1985. doi:10.1109/JLT.1985.1074188.
[12] Nasu Y, Kohtoku M, Hibino Y. Low-loss waveguides written with a femtosecond laser for flexible interconnection in a planar light-wave circuit. Opt. Lett. 2005. doi:10.1364/ol.30.000723.
[13] Xia Cen, Eftekhar MAmin, Correa Rodrigo Amezcua, Antonio-Lopez Jose Enrique, Schülzgen Axel, Christodoulides Demetrios, Li Guifang. Supermodes in Coupled Multi-Core Waveguide Structures. IEEE J. Sel. Top. Quantum Electron. 2016. doi:10.1109/JSTQE.2015.2479158.
[14] Chan FYM, Lau APT, Tam H-Y. Mode coupling dynamics and communication strategies for multi-core fiber systems. Opt. Express 2012. doi:10.1364/oe.20.004548.
[15] Snyder AW. COUPLED-MODE THEORY FOR OPTICAL FIBERS. J Opt Soc Am 1973. doi:10.1364/josa.62.001267.
[16] Schermer RT, Cole JH. Improved bend loss formula verified for optical fiber by simulation and experiment. IEEE J. Quantum Electron. 2007. doi:10.1109/JQE.2007.903364.
[17] Arrizabalaga Oskar, Sun Qi, Beresna Martynas, Lee Timothy, Zubia Joseba, Pascual Javier Velasco, Ocáriz Idurre Sáez de, Schülzgen Axel, Antonio-Lopez Jose Enrique, Amezcua-Correa Rodrigo, Villatoro Joel, Brambilla Gilberto. High-performance vector bending and orientation distinguishing curvature sensor based on asymmetric coupled multi-core fibre. Sci. Rep. 2020. doi:10.1038/s41598-020-70999-8.
[18] Landi G. Properties of the center of gravity as an algorithm for position measurements. Nucl. Instruments Methods Phys. Res. Sect. A Accel. Spectrometers, Detect. Assoc. Equip. 2002;485(3). doi:10.1016/S0168-9002(01)02071-X.
[19] Landi G. Properties of the center of gravity as an algorithm for position measurements: Two-dimensional geometry. Nucl. Instruments Methods Phys. Res. Sect. A Accel. Spectrometers, Detect. Assoc. Equip. 2003;497(2–3). doi:10.1016/S0168-9002(02)01822-3.
[20] Yin Y, Qiao Y, Hu S. Four-point bending tests for the fracture properties of concrete. Eng. Fract. Mech. 2019;211. doi:10.1016/j.engfracmech.2019.03.004.
[21] *Advances in Mechanical Systems Dynamics*. 2020.